Mechanical response and yielding transition of silk-fibroin and silk-fibroin/cellulose nanocrystals composite gels

Mechanical response and yielding transition of silk-fibroin and silk-fibroin/cellulose nanocrystals composite gels

G. Poggi[1], D. Chelazzi[1], M. Laurati[1*]

[1]*Department of Chemistry "Ugo Schiff" and CSGI, University of Florence, Via della Lastruccia 3, 50019, Sesto Fiorentino, Florence, Italy.*

Abstract

We investigated the mechanical properties of gels formed by silk fibroin and silk fibroin/cellulose nanocrystal mixtures. Viscosity and linear viscoelasticity measurements showed that the addition of cellulose nanocrystals induces a speed-up of the gelation kinetics and leads to moderately stiffer gels. Combining continuous shear tests and large amplitude oscillatory shear (LAOS) measurements we additionally characterized the shear-induced solid-fluid transition. Continuous shear tests indicated a larger yield stress for the silk fibroin/cellulose nanocrystal gel, confirming thus the stiffening effect. They also revealed that the yield strain of the gels becomes smaller at higher shear rates, possibly as a result of shear-induced compaction. The detailed analysis of the full anharmonic response in LAOS measurements additionally evidenced that the fluidization of the gels is a broad and gradual transition, which is characterized by two different yield strains: one corresponding to the onset of solid melting and one to the complete fluidization of the system.

Keywords: Fibroin gel, rheology, cellulose nanocrystal, yielding

1. Introduction

The development of sustainable biomaterials and green composites is at the forefront of the research efforts in materials science [1, 2]. Sustainable, eco-friendly biomaterials find already application in cancer therapy, orthopedic implants, contact lenses, breast implants, among others. Similarly, composite materials based on biopolymers and natural fibers help solving problems related with the disposal and/or recycling of synthetic polymers and fibers, the high energy cost of their fabrication and the limited reserves of petroleum, which is at the basis of their production. Green composites find use as insulating materials, as panelling for the automotive industry, and as housing for electronic components, among others.

A fundamental aspect of the performance of these two classes is their mechanical response, which determines their flexibility, toughness, strength and durability [3, 4].

*Corresponding author

Email address: marco.laurati@unifi.it (M. Laurati[1])

Silk fibroin is an abundant natural protein produced by silkworms and spiders. For applications as biomaterial and in composites, fibroin protein fibers have the advantage of presenting a high mechanical strength [5, 6]. Fibroin solutions, which are initially in a fluid state, spontaneously undergo gelation following a two-step process [7, 8]: during early stage gelation, initial network formation is driven by hydrogen bonding, hydrophobic interactions and electrostatic interactions, without changes in the secondary structure; later, strong interactions occur leading to the formation of an increasingly larger fraction of β-sheets which lead to mechanically stable hydrogels [9]. The fibroin concentration and the processing conditions strongly affect the degree of crosslinking and the bond strength, thus the mechanical response of the gel [8]. A few studies investigated also the non-linear rheological response of fibroin solutions and gels, showing the presence of strain hardening effects at sufficiently large fibroin concentration [10, 11, 12, 13, 14]. Additionally, the gelation kinetics, which are typically slow [15], are particularly sensitive to pH, temperature and ionic strength [7, 16]. The mechanical properties of fibroin gels can be also tuned through the addition of a second component, which can be a synthetic polymer like polyacrylamide [17], polyethylene oxide [15], polyvinyl alcohol [18] or polyurethane [19], or a natural polymer, like collagen [20], chitosan [21], pectin [22] or alginate [23], among others. There are also a few examples of the use of cellulose nanofibers (CNF) and cellulose nanocrystals (CNC) combined with fibroin to obtain all-natural composite materials [24, 25, 26, 27, 28]. For instance, we recently proposed the use of dispersions of self-regenerated silk fibroin (SRSF) extracted from Bombyx mori for the consolidation of fragile silk fibers [29, 30]. To further increase the spectrum of fine adjustment of the mechanical properties of the dispersions, and thus better meet the needs of silk conservators, SRSF was blended with CNC.

The composition and processing conditions of the composite fibroin gels investigated in the mentioned studies are typically very diverse and specifically tailored towards desired applications: it is thus difficult to draw any general conclusion on the effect of the addition of nanocellulose on the mechanical behavior of these systems. Moreover, mechanical characterization was mainly focused on the measurement of linear viscoelasticity and viscosity, while the yielding transition of the materials remained essentially unexplored. Such transition is of primary interest for processing and application purposes. To fill this knowledge gap, we compare in this work the mechanical response of gels formed by pure SRSF dispersions and by SRSF/CNC mixtures with the same content of SRSF. By combining different rheological techniques and analysis methods, we determine the viscosity and stiffness of the gels, and we characterize in great detail the yielding transition. Our findings show that the addition of CNC alters the gelation kinetics, leads to stronger gels and qualitatively modifies the yielding behavior. In addition, by applying the sequence of physical processes (SPP) approach [31, 32] to the analysis of large amplitude oscillatory strain (LAOS) measurements, we find evidence of a broad yielding transition for both gels, which is characterized by a progressive fluidization for which we precisely determine the characteristic strain at which this process starts and the one at which it is almost complete.

2. Materials and Methods

2.1. Materials

Ethanol (EtOH, analytical grade, Carlo Erba), calcium chloride (dehydrated $CaCl_2$ (powder; > 97.0% (KT), Fluka), and cellulose nanocrystals, commercial white taffetà silk (Casa del tessuto, Florence), CNC (0.7–0.8% of residual sulfur, Celluforce), were used for the preparation of the SRSF and hybrid SRSF-CNC dispersions. Silver nitrate ($AgNO_3$, 0.1M, Merck) was used for chloride assays. Ultrapure Milli-Q water (resistivity: 18.2 MΩ·cm at 25 °C) was used where needed. The SRSF dispersions were obtained from taffetà silk, using a modified version of the protocol reported elsewhere [30]. The silk textiles were washed with EtOH four times to remove impurities and industrial additives, and let dry at room temperature; then, the textile was immersed in a solution of $CaCl_2$:H2O:EtOH (molar ratio of 1:8:2), keeping a bath ratio of 0.1 g/mL. The bath was heated at 90 °C and stirred for 15 minutes. The solution was then dialyzed with a membrane cell (Dialysis tubing, high retention seamless cellulose tubing, MWCO 12400, 99.9% retention, Sigma Aldrich) for 48 hours against 1 L water. Water was changed four times, and the dialysis bath was kept under magnetic stirring to facilitate the desalination process. The effective elimination of the salt was verified through $AgNO_3$ chloride assays. The dialyzed solution was centrifuged twice at 9000 rpm for ten minutes, and the supernatant separated. The final concentration of fibroin in the dispersion (2.70% w/v) was measured gravimetrically by weighting 1000 μL of dispersion before and after complete drying. The fibroin dispersion was then diluted to 0.15% w/v. Aqueous CNC dispersions were prepared by magnetic stirring CNC powder into water for 5 h at room temperature. The dispersions were then ultrasonified for 5 minutes with 20% amplitude, using a Branson S-450 ultrasonifier equipped with micro-tip. A concentration of 0.15% was prepared. SRSF/CNC hybrid dispersions were prepared by mixing and magnetically stirring CNC and SRSF dispersions at the moderate speed of 300 rpm, obtaining the total concentration 0.15%/0.15% w/v. The prepared dispersions are neutral (pH 6.5-7.0). The selected SRSF and CNC concentrations were found to be particularly effective in preserving aged and fragile silk textiles, while avoiding gelation of CNC that prevents practical application of the dispersions. Measurements were performed at different waiting times after sample preparation, as detailed in section 3.

2.2. Rheology

Rheological measurements were performed with a DHR3 hybrid rheometer (TA Instruments) using a 40mm smooth cone-plate geometry. Sample evaporation was found to be negligible over the duration of the experiments, as determined from repeated tests performed at different waiting times after sample loading. The temperature of the bottom plate was controlled through a Peltier heating/cooling system and was set to T = 20 °C. Flow curves were measured for 10 $s^{-1} < \dot{\gamma} < 500$ s^{-1} using an equilibration time of 10 s and an averaging time of 30 s. Step rate experiments were performed for $\dot{\gamma} = 0.1$, 0.5, 1.0, 5.0 and 10.0 s^{-1} and creep tests for applied stresses $\sigma = 0.10$, 0.30, 0.50, 0.70 and 1.00 Pa. Dynamic frequency sweeps were measured for a strain amplitude $\gamma_0 = 1.0\%$, which lies within the linear response regime, see Fig.6. Each measured point is the result of averaging over 3 cycles of oscillation. Finally, Dynamic

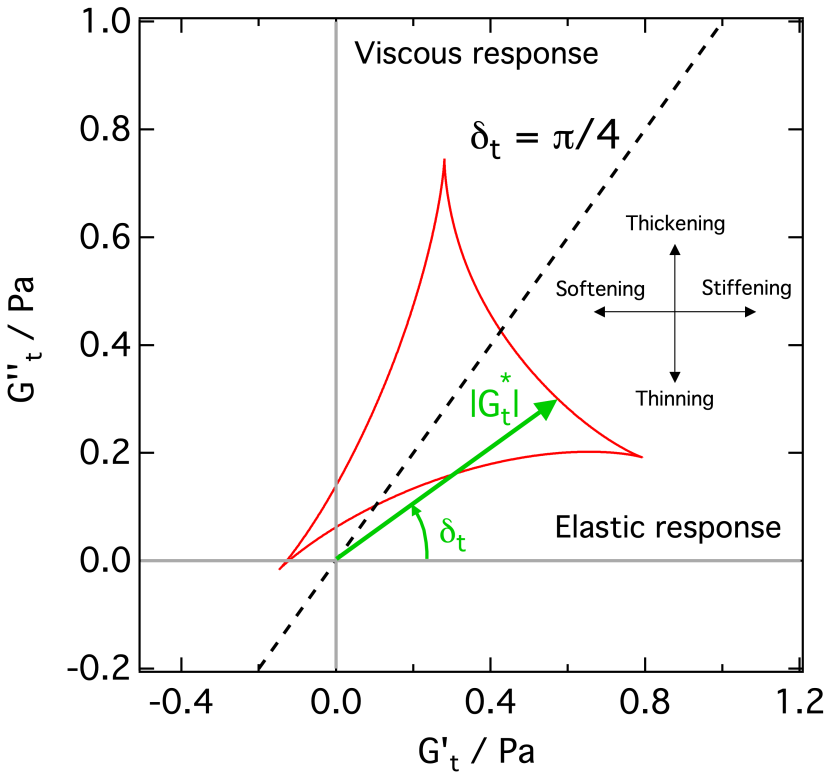

Figure 1: Exemplary Cole-Cole plot illustrating the meaning of δ_t and $|\,G_t^*\,|$, as well as the in-cycle yielding criterion. Each value along the Cole-Cole curve corresponds to a value of the instantaneous moduli, which together determine the modulus of $|\,G_t^*\,|$. δ_t quantifies the ratio between viscous and elastic contributions. When the value of $\delta_t = \pi/4$ is exceeded, the material transitions from a dominant elastic to a dominant viscous response, therefore yielding. Directions of in-cycle stiffening/softening and thickening/thinning are indicated by black arrows.

strain sweeps were measured for $\omega_0 = 1.0$ rad/s and increasing strain amplitude. Measurements at each strain amplitude were averaged over 3 cycles and the raw strain and stress signal were recorded and analyzed as described in the following section. Since the kinetics of gel formation in these samples is extremely slow, as will be shown in the Results and Discussion section, i.e. gel structures form over times considerably longer than a day, no rejuvenation protocol could be used. The different tests were thus performed each time on new samples having the same age with respect to the preparation time. Samples were fxreshly loaded following the same protocol. Error bars on the rheological data are smaller than the symbol size.

2.3. SPP analysis

During dynamic strain sweeps the raw stress and strain signals were recorded. These were later analyzed according to the SPP approach using the MATLAB-based SPPplus analysis software [32]. The SPP technique has been described in detail in previous work by Rogers and coworkers [31, 33]. We report here a brief description of the most important concepts and of the parameters used for analyzing yielding in the SRSF and SRSF/CNC samples.

The SPP approach describes the rheological response to oscillatory shear as a closed three-dimensional space curve in strain, rate and stress space. For each point on the curve, a Frenet-Serret frame[34, 35] can be defined by introducing a set of three orthonormal vectors: the tangent **T**, normal **N** and binormal **B** vectors, which describe the instantaneous direction of motion, the instantaneous change in direction, and the cross product of these two. The projections of the binormal vector along the strain (γ), rate ($\dot{\gamma}/\omega$) and stress (σ) axes are used to define the instantaneous moduli G'_t and G''_t:

$$G'_t = -\frac{B_\gamma}{B_\sigma} \tag{1}$$

$$G''_t = -\frac{B_{\dot{\gamma}/\omega}}{B_\sigma} \tag{2}$$

For a linear rheological response the trajectory in the strain, rate, stress space is planar and the instantaneous moduli are constant within a cycle of oscillation. Instead, when the response becomes non-linear, the binormal vector **B** will change orientation during the cycle of oscillation and thus the instantaneous moduli will not any longer be constant and reflect the physical processes occurring in the material.

The instantaneous moduli of Eq.2 can be also used to define the complex instantaneous modulus $\mid G^*_t \mid$ and the phase angle δ_t, in analogy with the commonly used linear viscoelastic moduli:

$$\mid G^*_t \mid = \sqrt{G'^2_t + G''^2_t} \tag{3}$$

$$\delta_t = \tan^{-1}\left(\frac{G''_t}{G'_t}\right) \tag{4}$$

The interpretation of these parameters in terms of material yielding can be understood using Fig.1, which shows an exemplary Cole-Cole plot in which G''_t is reported vs. G'_t for an oscillation cycle at a certain oscillation amplitude γ_0 and frequency ω. The quantity $\mid G^*_t \mid$ represents the instantaneous magnitude of the viscoelastic response. The quantity δ_t, being the ratio between the instantaneous loss and storage moduli, is a measure of the solid-like or viscous-like response of a material: small values of δ_t indicate solid-like response while large values fluid-like response. The onset of in-cycle yielding can be therefore defined as the point at which the response changes from primarily elastic, $\delta_t < \pi/4$, to primarily viscous, $\delta_t > \pi/4$. The dashed line in Fig.1 indicates the location of the yielding points in the Cole-Cole representation of the rheological data. The directions of increasing/decreasing G'_t and G''_t indicate in-cycle stiffening/softening and thickening/thinning, respectively (Fig.1). Finally, to quantify the rate at which changes in the state of a material occur across yielding, the phase

angle velocity, $\dot{\delta}_t$ can be defined. Positive values of $\dot{\delta}_t$ will be associated to yielding, i.e. an increase from a small to a large value of δ_t, while negative values of $\dot{\delta}_t$ to reformation, i.e. a transition from a large to a small value of δ_t. For a sinusoidal applied deformation, $\dot{\delta}_t$ can be expressed as:

$$\dot{\delta}_t = \frac{-\omega\dot{\sigma}(\ddot{\sigma} + \omega^2\dot{\sigma})}{\ddot{\sigma} + \omega^2\dot{\sigma}^2} \tag{5}$$

and introducing a normalized time $\tilde{t} = \omega t$ we obtain a dimensionless form of $\dot{\delta}_t$ (which instead would have dimension t^{-1}):

$$\tilde{\dot{\delta}}_t = \frac{-\tilde{\dot{\sigma}}(\tilde{\ddot{\sigma}} + \tilde{\sigma})}{\tilde{\ddot{\sigma}} + \tilde{\dot{\sigma}}^2} \tag{6}$$

3. Results and Discussion

3.1. Continuous shear

3.1.1. Viscosity vs. structuring time

To assess the time-dependent microscopic structuring of the pure fibroin and composite samples, we investigated the dependency of the samples' viscosity extracted from flow curves (Fig.2a,b) on the time elapsed after sample preparation, which we call structuring time. Panel (a) of Fig.2 shows exemplary measurements obtained for samples after 11 days: while the CNC dispersion shows a Newtonian behavior with a constant viscosity, the SRSF and SRSF/CNC samples present a shear-thinning response and a yield stress. Note that for the CNC sample, data for $\dot{\gamma} < 60$ s^{-1} were omitted due to the large statistical noise. To monitor the evolution of the response as a function of the structuring time, we plot in panel (b) the high-shear viscosity, η_∞, estimated from the point of the flow curve at maximum shear rate, as a function of the structuring time. For the CNC sample η_∞ does not show any significant dependence on the structuring time, indicating that the system behaves at all times as a dilute suspension. On the other hand η_∞ for the SRSF and SRSF/CNC samples shows a pronounced increase as a function of the structuring time, reaching values 6-times (SRSF) and 4-times (SRSF/CNC) higher than the initial values after 15 days. The viscosity grows faster at the beginning for the SRSF/CNC sample, but slower at longer times, leading to a final viscosity that is lower compared to the SRSF sample. Observation of the sample structure with bright-field microscopy (Fig.2c) evidences the progressive formation of large scale aggregates in both samples, and the increase of structural heterogeneity. Note that for sample SRSF no clear large scale structure is developed after 5 days, while a certain structuring is already visible for SRSF/CNC, in agreement with the viscosity data. The observed structural features are characteristic of the formation of gel networks: similar structures were previously reported for SRSF samples [8]. As discussed in the introduction, gel formation in pure fibroin solutions is driven by initial bonding through weak interactions followed by a strong increase in the amount of β-sheet structures, which leads to a mechanically stable network. The viscosity data thus suggest that formation of β-sheet structures is faster in the SRSF/CNC composites than in pure SRSF solutions. To investigate this hypothesis we performed FTIR measurements right after

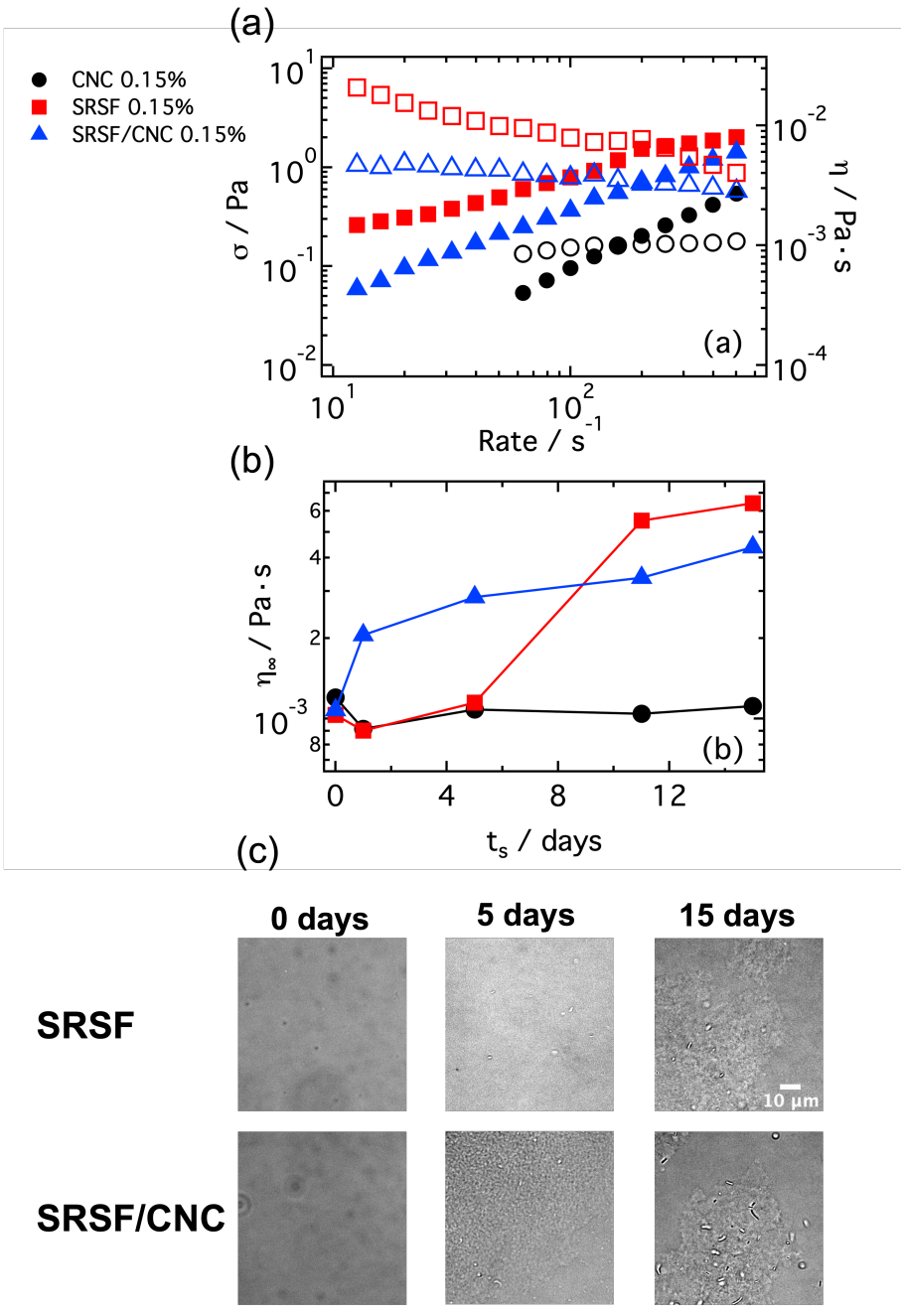

Figure 2: (a) Stress σ (left y-axis, full symbols) and viscosity η (right y-axis, open symbols) vs shear rate measured for CNC 0.15%, SRSF 0.15% and SRSF/CNC 0.15%/0.15% samples after 11 days, as indicated. (b) High shear viscosity η_∞ extracted from flow curves, as a function of structuring time (t_S) for the same samples as in (a). (c) Bright-field microscopy snapshots illustrating the structural evolution of the samples as a function of structuring time. A scale bar, which is equal for all images, is reported in the image of the SRSF sample measured after 15 days of structuring time.

sample preparation and at the structuring time of 1 day. The results, which are reported in Fig.S1 of the Supplementary Material, show that while the amount of β-sheet structures is similar in SRSF and SRSF/CNC at 0 structuring time, it increases significantly more in SRSF/CNC, leading thus to a faster structuring. Note also that the SRSF/CNC samples present a larger amount of α-helix structures. Additional discussion of the FTIR results can be found in the Supplementary Material. Further characterization of the structure at smaller length scales of SRSF and SRSF/CNC samples after 13 days was obtained by SAXS and is reported in the Supplementary Material. The SAXS data show that the SRSF network is formed by small fractal fibroin aggregates of average size $\xi \approx 65$ nm and fractal dimension $d_m \approx 1.8$. In the SRSF/CNC the network is also formed by aggregates, however with a slightly smaller average size, $\xi \approx 14$ nm and slightly large fractal dimension, $d_m \approx 2.0$. These results confirm that the mixing with CNC alters the structural evolution of the sample and network formation.

3.1.2. Stress Growth and Creep

Stress growth and creep tests were performed to investigate the yielding under continuous shearing of the gel structures formed in the SRSF and SRSF/CNC samples after 13 days of structuring time, which correspond to steady state gel structures (no significantly different behavior is expected compared to 15 days of structuring time). Fig.3a shows the stress σ vs. strain γ curves measured for the two samples under different applied shear rates $\dot{\gamma}$ in the range $0.1 \leq \dot{\gamma} \leq 10$ s^{-1}. Both samples show a qualitatively similar transient response characterized by an initial increase of the stress in the linear response regime followed by a stress overshoot, and later a tendency to a constant σ value characteristic of fluid flow. The stress overshoot indicates a yielding process associated with the breaking of the joints of the network structure. In colloidal gels it has been associated to bond breaking and cluster disruption [36, 37, 38, 39, 40, 41]. In our samples, the mechanical stability of the network is mainly due to the presence of β-sheet intermolecular structures, which are thus expected to break apart at the yield point. The strain at which the overshoot is observed provides therefore an estimate of the yield strain γ_y of the gel, and can be associated to a characteristic length scale in the microscopic structure of the samples. The stress at the overshoot is an estimate of the yield stress σ_y of the gel. The overshoot is observed at a strain $\gamma_y \approx 50$ % for the SRSF sample at rates $\dot{\gamma} = 1.0$ and 5.0 s^{-1}, while for $\dot{\gamma} = 10.0$ s^{-1} the presence of the overshoot is less clear, since for this high rate data at short times (strains) are affected by tool inertia[42]. For the SRSF/CNC samples the overshoot is observed at a comparable value γ_y for the smallest rate $\dot{\gamma} = 0.1$ s^{-1}, but shifts to increasingly smaller values for $\dot{\gamma} = 0.5$ and 1.0 s^{-1} (Fig.4a), indicating that the sample becomes more brittle with increasing $\dot{\gamma}$. At comparable rate, the yield strain γ_y is smaller for the SRSF/CNC sample (Fig.4a), indicating a different microscopic structure of the SRSF and SRSF/CNC gels, as suggested by SAXS.

The yield stresses of both samples increase with increasing shear rate (Fig.3a, Fig.4b), indicating that breaking of the network structure needs a larger amount of energy for higher shear rates. The yield stress of the SRSF/CNC sample is slightly larger than that of the pure SRSF sample. The amount of stress stored in the system during yielding and released when the system flows can be estimated from the relative height of the stress overshoot, which we define as $(\sigma_y - \sigma_p)/\sigma_p$, with σ_p the stress in the steady state

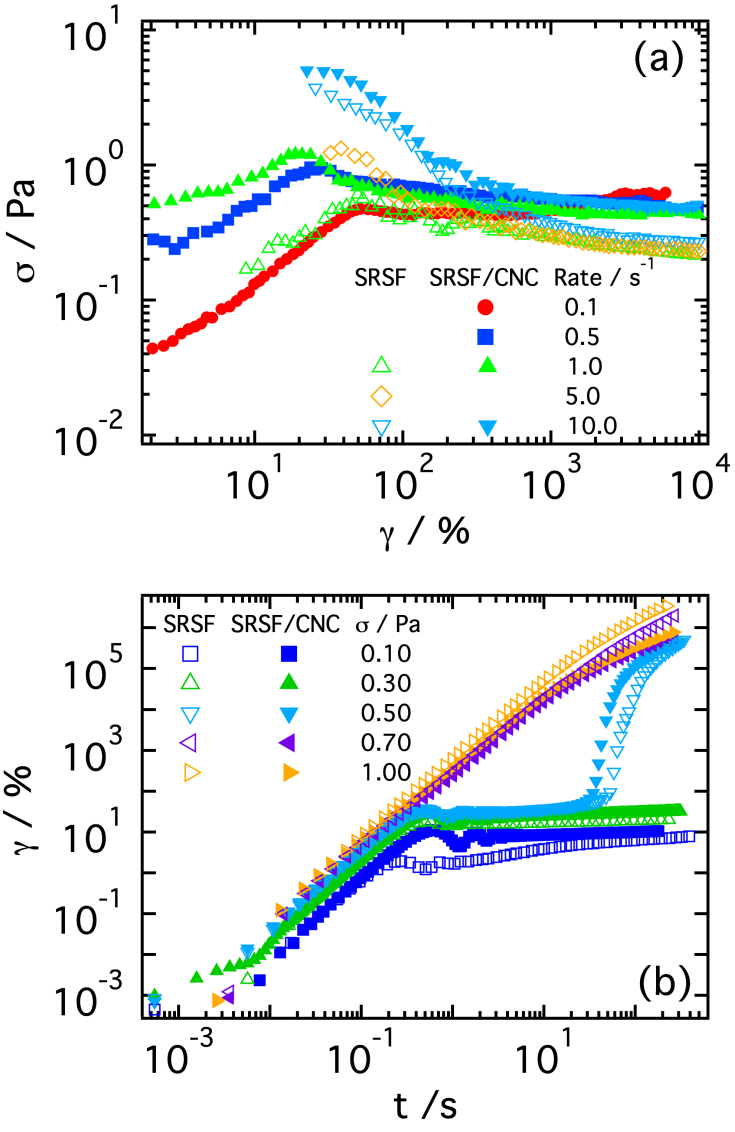

Figure 3: Stress σ vs strain γ from stress growth experiments (a) and strain γ vs. time t from creep experiments (b) performed on samples SRSF 0.15% and SRSF/CNC 0.15%/0.15% after 13 days. The applied shear rates and stresses are reported in legends.

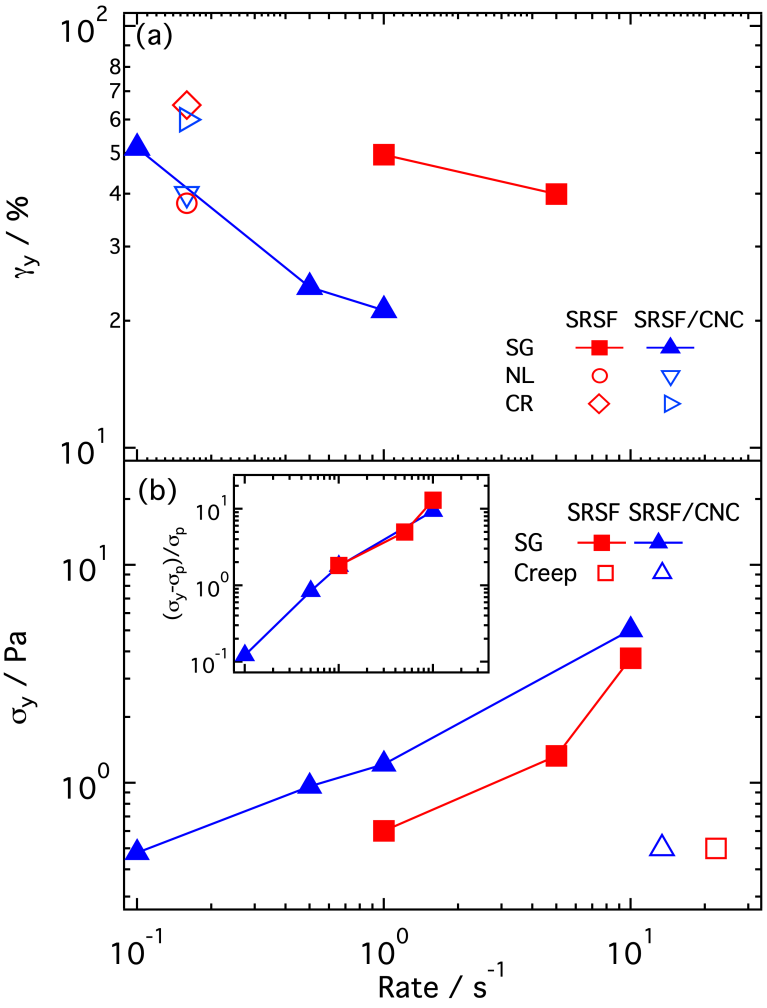

Figure 4: Yield strain γ_y (a) and yield stress σ_y (b) vs shear rate, extracted from the stress overshoot in stress growth experiments on samples SRSF 0.15% and SRSF/CNC 0.15%/0.15%. In (a) values of the yield strain obtained from the onset of non-linear regime (NL) and the crossover (CR) of the viscoelatic moduli in oscillatory dynamic strain sweeps are reported for comparison. The yield stress obtained from creep experiments is reported for comparison in panel (b) for the same samples. Inset in (b): amount of stress overshoot as a function of shear rate, same x-axis as the main plot.

of flow. The relative height of the overshoot increases with increasing rate, meaning that more stress is stored before the system yields. The two samples show comparable values of this quantity. This suggests that the larger yield stress of the SRSF/CNC sample is associated primarily to a larger elasticity of the gel network, which might be connected to changes in the aggregate size and fractal dimension evidenced by the SAXS measurements and also in recent work [43]. Measurements of the viscoelastic moduli presented in the next section confirm the increase of elasticity in the presence of CNC.

Fig.3b shows strain vs. time curves obtained from creep experiments for selected, different applied stresses. We neglect in what follows data for $t < 10^{-1}$ s, which are affected by tool inertia [44]. For small applied stresses the response of both samples is that of a creeping solid, with γ increasing slowly with increasing elapsed time t. The increase of γ is slightly slower for the SRSF sample. For large stresses the systems show a flowing behavior, with γ increasing linearly as a function of t at sufficiently long times. For intermediate stresses, like the curves for $\sigma = 0.50$ Pa in Fig.3b, a transition from creep to flow behavior is observed in the experimental time window, indicating yielding. As it can be seen the transition from creep to flow is sudden for both samples. We defined a yield stress in creep tests as the applied stress for which the strain vs. time curve shows for the first time a transition from creep to flow. The obtained values were reported in Fig.4b, using the value of the shear rate achieved when the system flows, i.e. at long times within the creep measurement. The yield stresses obtained from creep measurements are smaller than those determined from stress growth tests. This indicates that for these samples the application of stress is more effective than strain in rearranging the network structure [45].

3.2. Oscillatory shear

3.2.1. Linear Viscoelasticity

The linear viscoelastic moduli of the SRSF and SRSF/CNC gels (samples measured after 13 days) were detrmined by small amplitude oscillatory shear with a strain amplitude $\gamma_0 = 1\%$. They show the characteristic response of soft solid samples like gels and glasses (Fig.5a) [46, 47, 48]: the storage modulus $G'(\omega)$ is larger than the loss modulus $G''(\omega)$ for all frequencies and the gap between the moduli increases with decreasing ω. The moduli of the SRSF/CNC sample are slightly larger than those of the pure SRSF sample suggesting, as already discussed, a stiffening effect induced by the presence of the cellulose nanocrystals which lead to more compact fibroin aggregates at the nanoscale, as shown by the SAXS measurements and as observed before [43]. At the same time they present a more pronounced frequency dependence for $\omega > 1$ rad/s, which suggests that the moduli of the SRSF/CNC sample could present a crossover in the region $\omega > 40$ rad/s, at a smaller frequency compared to the SRSF sample. This different behavior might result from contributions of relaxation processes of CNC at high frequencies [49].

3.2.2. LAOS: Dynamic Strain Sweeps and Lissajous-Bowditch Plots

To explore the yielding behavior under oscillatory shear, dynamic strain sweeps at frequency $\omega_0 = 1.0$ rad/s were measured for both samples. For each strain amplitude

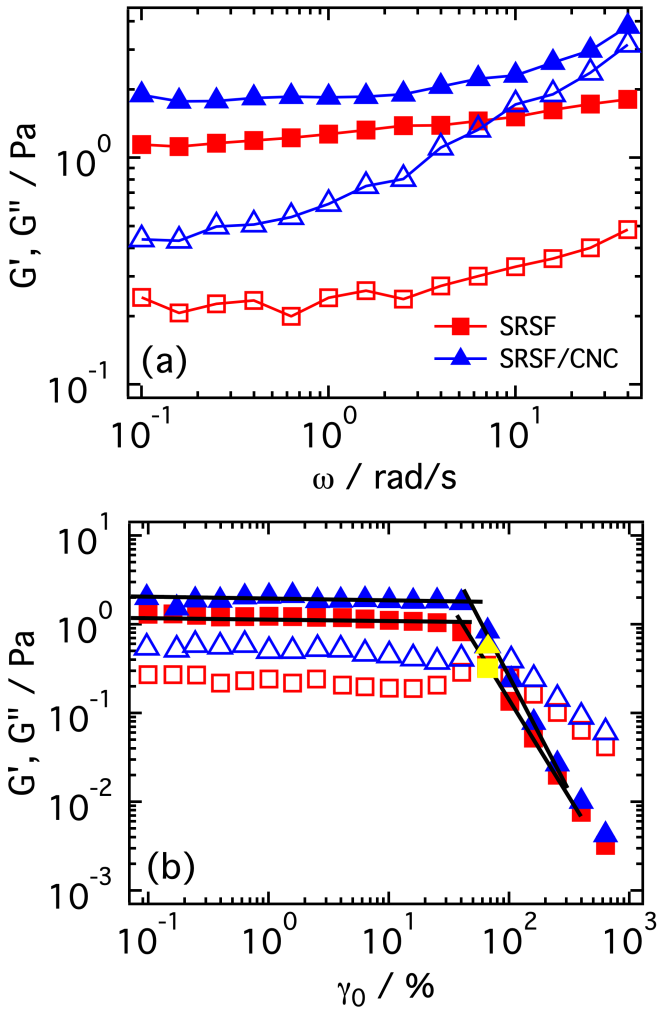

Figure 5: Storage G' and loss G'' moduli obtained for samples SRSF 0.15% and SRSF/CNC 0.15%/0.15%, for a structuring time of 13 days, as a function of (a) angular frequency ω, from SAOS measurements with $\gamma_0 = 1\%$ and (b) strain amplitude γ_0, from LAOS measurements at a frequency $\omega_0 = 1$ rad/s. The crossing point of the solid lines in (b) indicates the extrapolation of the transition from linear to non-linear response. The yellow symbols in (b) correspond to the maximum of G'' which also coincides with the crossover between G' and G''.

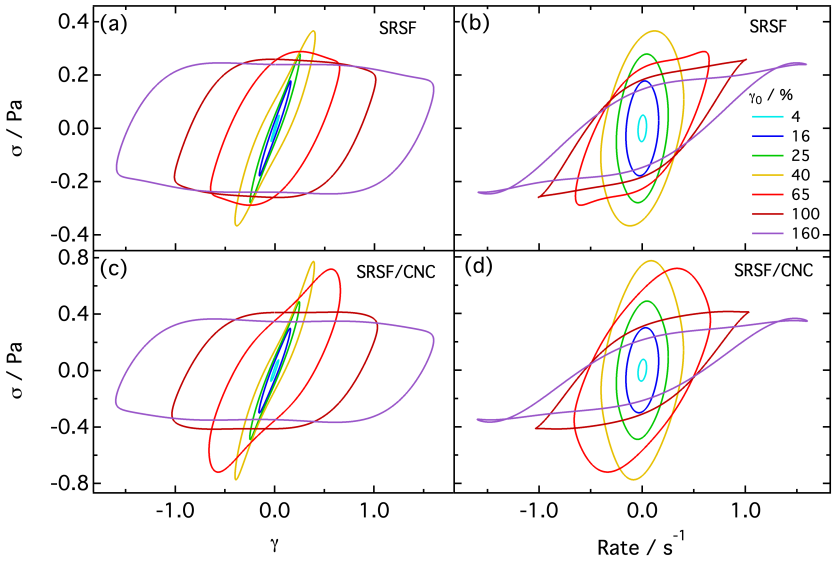

Figure 6: Elastic (a,c) and Viscous (b,d) Lissajous-Bowditch plots for samples SRSF 0.15% and SRSF/CNC 0.15%/0.15%, obtained from the raw stress, strain and strain rate signals measured in LAOS experiments with strain amplitudes $\gamma_0 = 4\%$, 16%, 25%, 40%, 65%, 100% 160%, from cyan to purple.

value along the strain sweep, the raw stress and strain data were additionally extracted for one cycle of oscillation. Fig.5b shows the amplitude-dependent moduli obtained in harmonic approximation directly from the rheometer. Additional analysis considering anharmonic contributions to the stress in the non-linear response regime will be presented in the next section. The moduli $G'(\gamma_0)$ and $G''(\gamma_0)$ obtained in harmonic approximation show a constant value in the linear viscoelastic response regime, followed by a decrease of G' and a simultaneous increase of G''. The onset of decrease of G' has been often used to define a yield strain γ_y^{NL} [36, 50, 51]. The two moduli reach a crossover, which also roughly coincides with the maximum of G''. This crossover corresponds apparently to the transition from solid-like to fluid-like response and to maximum dissipation (maximum of G''), and defines an alternative value for the yield strain γ_y^{CR} [52, 36, 50]. After the crossover, both moduli decrease as a function of increasing γ_0, following the fluidization of the sample. The values of γ_y^{NL} and γ_y^{CR} for the two samples are reported in Fig.4a: γ_y^{NL} is closely comparable to the yield strain estimated from step rate experiments, while γ_y^{CR} is larger. This suggests that significant network structure rearrangement takes place already at the onset of non-linear response: this will be confirmed by the SPP analysis. Additionally, at large amplitudes γ_0 the storage modulus $G' \sim \gamma_0^{\nu}$, with $\nu \approx -2.2$ for the SRSF sample, and $\nu \approx -2.3$ for the SRSF/CNC sample. According to recent work, for a slope $\nu = -2$ there is a constant average amount of energy stored per cycle [53]. Above yielding, any additional energy input is dissipated to the environment and does not contribute to internal

rearrangement of the structure. This suggests that the most energetically efficient flow condition can be obtained just above yielding, a result which shows analogies with the behavior of glassy mixtures of hard spheres [45].

Fig.6 shows elastic and viscous Lissajous-Bowditch curves [54, 55] extracted from the raw stress and strain signals measured within a cycle of oscillation for different strain amplitudes γ_0. Within the linear response regime the Lissajous-Bowditch figures of a viscoelastic material are expected to be elliptical and any deviation from the elliptical shape indicates the presence of higher-order harmonics in the response. We can observe that for $\gamma_0 = 4\%$ and 16% both elastic and viscous figures are indeed elliptical, confirming that the response is linear for these values of the strain amplitude. For $\gamma_0 = 25\%$ slight deviations from the elliptical shape are already visible: in particular in the elastic figure approaching the maximum strain amplitude, where shear reversal occurs, the stress increases in a slightly super-linear fashion, indicating the presence of strain hardening. For $\gamma_0 = 40\%$ the hardening response is further enhanced. Strain hardening effects have been observed in pure fibroin solutions with concentrations $\gtrsim$ 4% [10, 11, 12], and have been attributed to the shear-induced formation of transient intermolecular domains that act as additional cross-links [13]. While the concentration in our samples is much lower, at the extreme of the oscillation amplitude, before network yielding, this kind of phenomena may start to appear. When $\gamma_0 = 65\%$, while the response is still qualitatively similar for sample SRSF/CNC, it changes significantly for the pure SRSF sample: in the elastic figure, well before strain reversal the stress first flattens and then decreases presenting a maximum or overshoot similar to that observed in the stress growth experiments. In the viscous figure, the stress first flattens indicating shear thinning, which apparently is interrupted before shear reversal, since σ slightly increases as a function of $\dot{\gamma}$. For the two largest values of $\gamma_0 = 100\%$ and 160% the response indicates that the system flows over a large portion of the cycle, as indicated by the almost constant stress in the elastic figure. The flat parts in the viscous figure correspond to shear thinning behavior.

3.2.3. LAOS: SPP Analysis

The SPP analysis allows to get more detailed insight into the yielding transition under oscillatory shear, providing information on the dynamics of the mechanical response during a cycle of oscillation. Figs.7a,b show Cole-Cole plots of the instantaneous moduli G_t' and G_t'' for selected values of the strain amplitude $\gamma_0 = 25\%$, 40%, 65%, 100% and 160%. For $\gamma_0 = 25\%$ the curve for the SRSF samples lies almost entirely in the region below the $\delta_t = \pi/4$ line and therefore the sample response is still predominantly elastic over the entire oscillation cycle. The data for the SRSF/CNC samples lie even deeper inside the elastic region. When $\gamma_0 = 40\%$ the response of the two samples shows a marked difference: for the SRSF sample a large part of the curve lies above the $\delta_t = \pi/4$ line, i.e. the sample yields and is fluidized for a large portion of the cycle; the response of the SRSF/CNC sample instead still lies almost entirely within the elastic region. For larger values of γ_0 increasingly larger portions of the curves lie within the viscous region in correspondence to the progressive fluidization of the samples within a cycle. As it can be noticed, the fludization of the SRSF/CNC sample is delayed in terms of strain amplitude compared to the SRSF sample. A yield strain value can be estimated as the smallest value of the strain amplitude for which

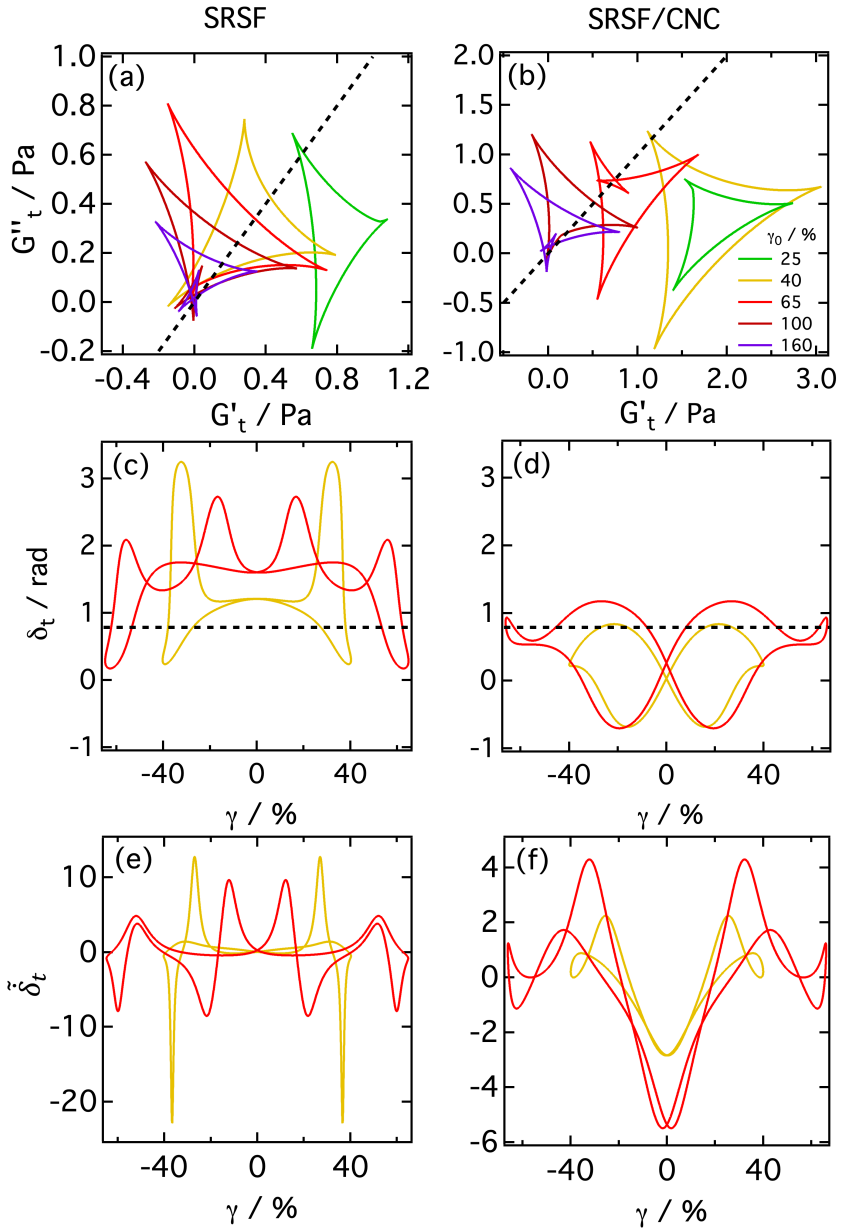

Figure 7: (a),(b) Cole-Cole plot of the instantaneous moduli G_t' and G_t'' (c),(d) instantaneous phase angle δ_t vs. strain γ, (e),(f) phase angle velocity $\tilde{\delta}_t$ vs. strain, obtained from SPP analysis applied to samples SRSF 0.15% (a,c,e) and SRSF/CNC 0.15%/0.15% (b,d,f).

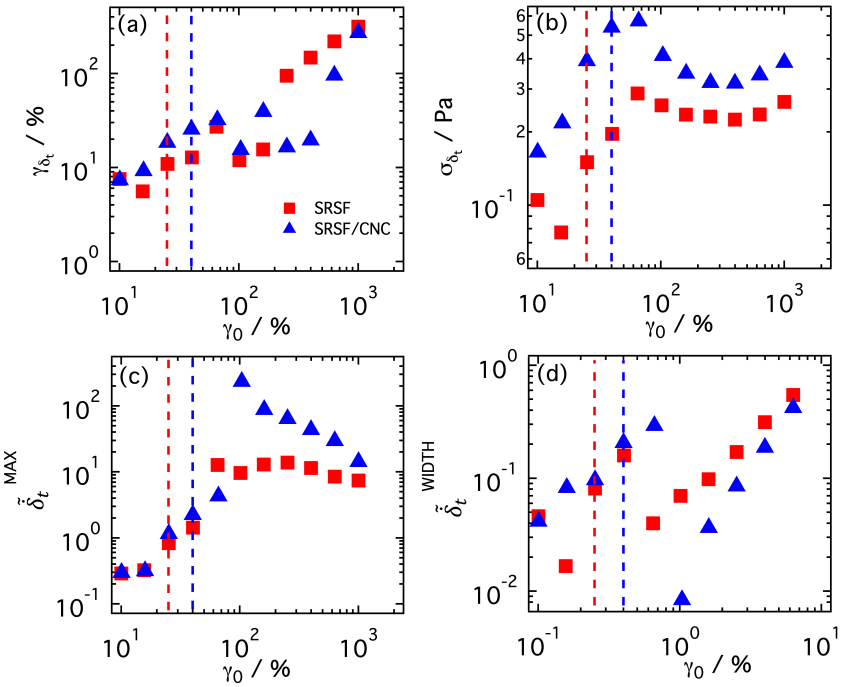

Figure 8: (a) Strain γ_{δ_t} and (b) stress σ_{δ_t} at which the primary maxima of $\tilde{\delta}_t$ are observed, and the corresponding height $\tilde{\delta}_t^{MAX}$ and width $\tilde{\delta}_t^{WIDTH}$ of the peaks, as a function of strain amplitude γ_0, for samples SRSF 0.15% and SRSF/CNC 0.15%/0.15%, as indicated. Dashed lines indicate the yield strain estimated from the Cole-Cole plots for the two samples.

at least a portion of the curve first crosses the $\delta_t = \pi/4$ line. According to this definition, we obtain values of $\gamma_y^{CC} = 25\%$ and 40% for samples SRSF and SRSF/CNC, respectively. These are smaller (SRSF) or comparable (SRSF/CNC) to the yield strain estimated as the onset of non-linearity in the moduli calculated in harmonic approximation. This result shows that already at the onset of non-linear response indicated by the moduli extracted in harmonic approximation, partial fluidization is present during a cycle of deformation. However, the average moduli calculated in harmonic approximation reflect the dominant response during a cycle. This confirms that only a detailed analysis of the in-cycle response allows to precisely identify the onset of fluidization. An additional estimate of the recoverable yield strain could be obtained in the limit of $G_t' \gg G_t''$ for large values of the strain amplitude[32], through the estimate of the elastic strain $\gamma_{el} \approx \sigma/G_t'$. Performing this calculation for the vertices with the highest G_t' value of the Cole-Cole diagrams in Fig.7 for $\gamma_0 = 100\%$ and 160% we obtained $\gamma_{el} \approx 17\%$ for SRSF and $\gamma_{el} \approx 20\%$ for SRSF/CNC, comparable but slightly smaller than the yield strains obtained in harmonic approximation.

Fig.7 reports in addition plots of the phase angle δ_t (panels c,d) and phase angle velocity $\tilde{\delta}_t$ (panels e,f) as a function of γ, for strain amplitudes $\gamma_0 = 40\%$ and 65%,

i.e. close to the yielding transition determined from the Cole-Cole analysis. Similar to what was discussed for Figs.7a,b, in cycle yielding occurs when $\delta_t > \pi/4$. Moreover, peaks in the phase angle correspond to largest ratios G_t''/G_t' and therefore indicate the maximal fluidization of the samples. The results in Figs.7c,d show that this occurs before the maximum strain amplitude is reached, and that for the SRSF sample, which presents a larger fluidization at comparable strain amplitude, it shifts to increasingly smaller values of γ. The peaks are relatively narrow and large for sample SRSF, while broad and small for sample SRSF/CNC.

The phase angle velocities $\dot{\tilde{\delta}}_t$ in Figs.7e,f are used to estimate the dynamics of the yielding transition around the peaks of δ_t. The positive peaks of $\dot{\tilde{\delta}}_t$, indicative of the main yielding transition, are particularly pronounced for sample SRSF and strain amplitude of 40%. The same data also show a rapid reformation of the sample structure after shear reversal (negative peaks).

We analysed in more detail the dynamics of yielding by extracting the values of the strain (γ_{δ_t}) and stress (σ_{δ_t}) at the main positive peaks of the $\dot{\tilde{\delta}}_t$ curves, as well as the height ($\dot{\tilde{\delta}}_t^{MAX}$) and width ($\dot{\tilde{\delta}}_t^{WIDTH}$) of the same peaks. Fig.8 shows these values as a function of the applied strain amplitude γ_0.

The in-cycle yield strain γ_{δ_t} is seen to increase initially with increasing γ_0 until $\gamma_0 =$ 65%: for larger values up to 160% or 300%, for SRSF and SRSF/CNC respectively, γ_{δ_t} remains approximately constant, with moderate fluctuations between $20\% < \gamma_{\delta_t} < 30\%$ (Fig.8a). For even larger γ_0 the values of γ_{δ_t} increase again. Note that $\gamma_0 = 65\%$ approximately corresponds to the strain amplitude at which a crossover between the moduli calculated in harmonic approximation, G' and G'', is observed. It is also the value for which a larger portion of the curves in the Cole-Cole plot occupies the viscous region. This result suggests therefore that there is a characteristic value of the in-cycle strain at which fluidization starts, $\gamma_{\delta_t}^* \approx$ 20-30%, and that above the crossover amplitude this value remains constant for a broad interval of strain amplitudes. Note that a strain amplitude of about 30% also corresponds to the onset of non-linear response in the amplitude sweeps, see Fig.5. This suggests that the in-cycle yielding is responsible for the increase in energy dissipation and the decrease of energy storage observed in the harmonic approximation. When the sample at the beginning of the test is already almost fluid, the value of γ_{δ_t} moves closer to the maximum strain amplitude. The stress corresponding to the peak of $\dot{\delta}_t$ shows even more clearly the qualitative change in the response of the gels around $\gamma_0 = 65\%$ (Fig.8b): For this value a maximum of σ_{δ_t} is found, similar to the stress overshoot in stress growth experiments. Thus stress accumulation grows until fluid-like behavior becomes dominant over a single cycle and later decays according to an almost complete fluidization of the sample. In the fluidized sample σ_{δ_t} is approximately constant. The height of the peak, $\dot{\tilde{\delta}}_t^{MAX}$, is also growing up to the same characteristic value and then remains constant (SRSF) or decreases (SRSF/CNC). This tells us that the velocity of the transition increases up to $\gamma_0 = 65\%$ and then stabilizes since the sample is already fluid-like. Interestingly, the width of the peak, $\dot{\tilde{\delta}}_t^{WIDTH}$, which indicates how broad is the transition in terms of applied strain amplitude, presents instead a discontinuity around the same value of γ_0: the width grows up to that value, then it suddenly drops and finally increases again.

This behavior is reminiscent of a first order transition [56]. Summarizing, the onset of non-linear response in harmonic approximation roughly coincides with the first value of γ_0 for which a small portion of the cycle presents a predominantly viscous response. Instead, the crossing of G' and G'' is instead comparable to the value of γ_0 for which, for the first time, the majority of the cycle is predominantly viscous. i.e the sample is completely fluidized.

4. Conclusions

We investigated the mechanical response of gels formed by self-regenerated silk fibroin and its mixture with cellulose nano-crystals, with a particular focus on the yielding transition. Measurements of the high shear viscosity as a function of structuring time show that the gelation kinetics become faster with addition of CNC: comparison with FTIR data shows that this is the result of the formation of a larger fraction of β-sheet structures in the SRSF/CNC composites. At the end of the structuring time both gels present weak solid structures characterized by storage moduli and yield stresses of the order of Pas, with both quantities being slightly larger for the SRSF/CNC gel. The larger storage modulus and yield stress of the SRSF/CNC gel can be associated with the formation of more compact fibroin aggregates at the nanoscale and to a larger content of β-sheet structures. We additionally found that while the yield stress increases with increasing $\dot{\gamma}$, the yield strain decreases. We speculate that this indicates a shear-induced compaction of β-sheet bonding structures at higher shear rates, which need a larger stress but smaller strain to be broken.
The analysis of the yielding process from LAOS measurements in first harmonic approximation allows to extract two distinct estimates of the yield strain: one corresponding to the onset of non-linear response, at $\gamma_y \approx 40\%$, which is comparable to results of step rate tests, and a second to the crossover of G' and G'', at $\gamma_y \approx 65\%$. A detailed analysis of the in-cycle yielding through the SPP approach, sheds light on the difference between these two estimates: the onset of non-linear response is the point at which the fluidization process begins, while the crossing of G' and G'' is the end of the process, corresponding to a major fluidization of the sample which is reflected in a stress maximum and a maximum velocity and width of the solid-fluid yielding transition. The entire fluidization process thus spans a broad range of strain amplitudes. The SPP analysis also reveals that when the system becomes predominantly viscous (for $\gamma_0 > 65\%$), the onset of the solid-fluid transition always occurs at a similar in-cycle strain of about 20-30%. Our study evidences that a detailed analysis of the mechanical properties and yielding behavior of complex gel structures, like those formed by SRSF/CNC dispersions, is of fundamental importance to design adequate processing conditions in applications, such as the consolidation of silk artworks.

Acknowledgments

We thank S. Rogers for providing the codes for the SPP analysis and for stimulating discussions. We acknowledge financial support from CSGI.

Data Availability Statement

The data that support the findings of this study are available from the corresponding author upon reasonable request.

References

[1] T. Biswal, S. K. Badjena, D. Pradhan, Sustainable biomaterials and their applications: A short review, Mater. Today: Proc. 30 (2020) 274–282, national Conference on "Trends in Minerals & Materials Technology". doi:https://doi.org/10.1016/j.matpr.2020.01.437.
URL https://www.sciencedirect.com/science/article/pii/S2214785320305423

[2] H. S. Shekar, M. Ramachandra, Green composites: A review, Mater. Today: Proc. 5 (1, Part 3) (2018) 2518–2526, international Conference on Advanced Materials and Applications (ICAMA 2016), June 15-17, 2016, Bengaluru, Karanataka, INDIA. doi:https://doi.org/10.1016/j.matpr.2017.11.034.
URL https://www.sciencedirect.com/science/article/pii/S2214785317322666

[3] M. A. Meyers, P.-Y. Chen, A. Y.-M. Lin, Y. Seki, Biological materials: Structure and mechanical properties, Prog. Mater. Sci. 53 (1) (2008) 1–206. doi:https://doi.org/10.1016/j.pmatsci.2007.05.002.
URL https://www.sciencedirect.com/science/article/pii/S0079642507000254

[4] M. P. Dicker, P. F. Duckworth, A. B. Baker, G. Francois, M. K. Hazzard, P. M. Weaver, Green composites: A review of material attributes and complementary applications, Compos. - A: Appl. Sci. Manuf. 56 (2014) 280–289. doi:https://doi.org/10.1016/j.compositesa.2013.10.014.
URL https://www.sciencedirect.com/science/article/pii/S1359835X13002893

[5] J. Gosline, P. Guerette, C. Ortlepp, K. Savage, The mechanical design of spider silks: from fibroin sequence to mechanical function, J. Exp. Biol. 202 (23) (1999) 3295–3303. arXiv:https://journals.biologists.com/jeb/article-pdf/202/23/3295/1235956/3295.pdf, doi:10.1242/jeb.202.23.3295.
URL https://doi.org/10.1242/jeb.202.23.3295

[6] X. Qiao, R. Miller, E. Schneck, K. Sun, Foaming properties and the dynamics of adsorption and surface rheology of silk fibroin at the air/water interface, Coll. Surf. A 591 (2020) 124553. doi:https://doi.org/10.1016/j.colsurfa.2020.124553.
URL https://www.sciencedirect.com/science/article/pii/S0927775720301461

[7] A. Matsumoto, J. Chen, A. L. Collette, U.-J. Kim, G. H. Altman, P. Cebe, D. L. Kaplan, Mechanisms of silk fibroin solgel transitions, J. Phys. Chem. B 110 (2006) 21630–21638. doi:10.1021/jp056350v.
URL https://doi.org/10.1021/jp056350v

[8] S. Kapoor, S. C. Kundu, Silk protein-based hydrogels: Promising advanced materials for biomedical applications, Acta Biomater. 31 (2016) 17–32. doi:https://doi.org/10.1016/j.actbio.2015.11.034.
URL https://www.sciencedirect.com/science/article/pii/S1742706115302105

[9] S. Nagarkar, A. Patil, A. Lele, S. Bhat, J. Bellare, R. A. Mashelkar, Some mechanistic insights into the gelation of regenerated silk fibroin sol, Ind. amp; Eng. Chem. Res. 48 (17) (2009) 8014–8023. doi:10.1021/ie801723f.
URL https://doi.org/10.1021/ie801723f

[10] A. Matsumoto, A. Lindsay, B. Abedian, D. L. Kaplan, Silk fibroin solution properties related to assembly and structure, Macromol. Biosci. 8 (11) (2008) 1006–1018. arXiv:https://onlinelibrary.wiley.com/doi/pdf/10.1002/mabi.200800020, doi:https://doi.org/10.1002/mabi.200800020.
URL https://onlinelibrary.wiley.com/doi/abs/10.1002/mabi.200800020

[11] X. Chen, D. P. Knight, F. Vollrath, Rheological Characterization of Nephila Spidroin Solution, Biomacromolecules 3 (4) (2002) 644–648. doi:10.1021/bm0156126.
URL https://doi.org/10.1021/bm0156126

[12] A. Ochi, K. S. Hossain, J. Magoshi, N. Nemoto, Rheology and Dynamic Light Scattering of Silk Fibroin Solution Extracted from the Middle Division of Bombyx mori Silkworm, Biomacromolecules 3 (6) (2002) 1187–1196. doi:10.1021/bm020056g.
URL https://doi.org/10.1021/bm020056g

[13] Z. Oztoprak, O. Okay, Reversibility of strain stiffening in silk fibroin gels, Int. J. Biol. Macromol. 95 (2017) 24–31. doi:https://doi.org/10.1016/j.ijbiomac.2016.11.034.
URL https://www.sciencedirect.com/science/article/pii/S0141813016310017

[14] A. P. Tabatabai, D. L. Kaplan, D. L. Blair, Rheology of reconstituted silk fibroin protein gels: the epitome of extreme mechanics, Soft Matter 11 (2015) 756–761. doi:10.1039/C4SM02079K.
URL http://dx.doi.org/10.1039/C4SM02079K

[15] U.-J. Kim, J. Park, C. Li, H.-J. Jin, R. Valluzzi, D. L. Kaplan, Structure and Properties of Silk Hydrogels, Biomacromolecules 5 (3) (2004) 786–792. doi:10.1021/bm0345460.
URL https://doi.org/10.1021/bm0345460

[16] A. Motta, C. Migliaresi, F. Faccioni, P. Torricelli, M. Fini, R. Giardino, Fibroin hydrogels for biomedical applications: preparation, characterization and in vitro cell culture studies, J. Biomater. Sci. Polym. Ed. 15 (7) (2004) 851–864. doi:10.1163/1568562041271075.
URL https://doi.org/10.1163/1568562041271075

[17] B. B. Mandal, S. Kapoor, S. C. Kundu, Silk fibroin/polyacrylamide semi-interpenetrating network hydrogels for controlled drug release, Biomaterials 30 (14) (2009) 2826–2836. doi:https://doi.org/10.1016/j.biomaterials.2009.01.040.
URL https://www.sciencedirect.com/science/article/pii/S0142961209000908

[18] J. Kundu, L. A. Poole-Warren, P. Martens, S. C. Kundu, Silk fibroin/poly(vinyl alcohol) photocrosslinked hydrogels for delivery of macromolecular drugs, Acta Biomater. 8 (5) (2012) 1720–1729. doi:https://doi.org/10.1016/j.actbio.2012.01.004.
URL https://www.sciencedirect.com/science/article/pii/S1742706112000116

[19] J. Hu, B. Chen, F. Guo, J. Du, P. Gu, X. Lin, W. Yang, H. Zhang, M. Lu, Y. Huang, G. Xu, Injectable silk fibroin/polyurethane composite hydrogel for nucleus pulposus replacement, J. Mater. Sci.: Mater. Med. 23 (3) (2012) 711–722. doi:10.1007/s10856-011-4533-y.
URL https://doi.org/10.1007/s10856-011-4533-y

[20] Q. Lv, K. Hu, Q. Feng, F. Cui, Fibroin/collagen hybrid hydrogels with crosslinking method: Preparation, properties, and cytocompatibility, J. Biomed. Mater. Res. 84A (1) (2008) 198–207. doi:https://doi.org/10.1002/jbm.a.31366.
URL https://doi.org/10.1002/jbm.a.31366

[21] X. Chen, W. Li, W. Zhong, Y. Lu, T. Yu, pH sensitivity and ion sensitivity of hydrogels based on complex-forming chitosan/silk fibroin interpenetrating polymer network, J. App. Polym. Sci. 65 (11) (1997) 2257–2262. doi:https://doi.org/10.1002/(SICI)1097-4628(19970912)65:11<2257::AID-APP23>3.0.CO;2-Z.
URL https://doi.org/10.1002/(SICI)1097-4628(19970912)65:11%3C2257::AID-APP23%3E3.0.COhttp://2-z

[22] K. Numata, S. Yamazaki, T. Katashima, J.-A. Chuah, N. Naga, T. Sakai, Silk-Pectin Hydrogel with Superior Mechanical Properties, Biodegradability, and Biocompatibility, Macromol. Biosci. 14 (6) (2014) 799–806. doi:https://doi.org/10.1002/mabi.201300482.
URL https://doi.org/10.1002/mabi.201300482

[23] K. Ziv, H. Nuhn, Y. Ben-Haim, L. S. Sasportas, P. J. Kempen, T. P. Niedringhaus, M. Hrynyk, R. Sinclair, A. E. Barron, S. S. Gambhir, A tunable silk–alginate hydrogel scaffold for stem cell culture and

transplantation, Biomaterials 35 (12) (2014) 3736–3743. doi:https://doi.org/10.1016/j.biomaterials.2014.01.029.
URL https://www.sciencedirect.com/science/article/pii/S0142961214000313

[24] J. Huang, L. Liu, J. Yao, Electrospinning of Bombyx mori silk fibroin nanofiber mats reinforced by cellulose nanowhiskers, Fibers Polym. 12 (8) (2011) 1002–1006. doi:10.1007/s12221-011-1002-7.
URL https://doi.org/10.1007/s12221-011-1002-7

[25] Y. Feng, X. Li, M. Li, D. Ye, Q. Zhang, R. You, W. Xu, Facile Preparation of Biocompatible Silk Fibroin/Cellulose Nanocomposite Films with High Mechanical Performance, ACS Sustain. Chem. Eng. 5 (7) (2017) 6227–6236. doi:10.1021/acssuschemeng.7b01161.
URL https://doi.org/10.1021/acssuschemeng.7b01161

[26] J. Chen, A. Zhuang, H. Shao, X. Hu, Y. Zhang, Robust silk fibroin/bacterial cellulose nanoribbon composite scaffolds with radial lamellae and intercalation structure for bone regeneration, J. Mater. Chem. B 5 (20) (2017) 3640–3650. doi:10.1039/C7TB00485K.
URL http://dx.doi.org/10.1039/C7TB00485K

[27] P. Dorishetty, R. Balu, S. S. Athukoralalage, T. L. Greaves, J. Mata, L. de Campo, N. Saha, A. C. W. Zannettino, N. K. Dutta, N. R. Choudhury, Tunable Biomimetic Hydrogels from Silk Fibroin and Nanocellulose, ACS Sustain. Chem. Eng. 8 (6) (2020) 2375–2389. doi:10.1021/acssuschemeng.9b05317.
URL https://doi.org/10.1021/acssuschemeng.9b05317

[28] R. Xiong, H. S. Kim, S. Zhang, S. Kim, V. F. Korolovych, R. Ma, Y. G. Yingling, C. Lu, V. V. Tsukruk, Template-Guided Assembly of Silk Fibroin on Cellulose Nanofibers for Robust Nanostructures with Ultrafast Water Transport, ACS Nano 11 (12) (2017) 12008–12019. doi:10.1021/acsnano.7b04235.
URL https://doi.org/10.1021/acsnano.7b04235

[29] D. Badillo-Sanchez, D. Chelazzi, R. Giorgi, A. Cincinelli, P. Baglioni, Characterization of the secondary structure of degummed Bombyx mori silk in modern and historical samples, Polym. Degrad. Stab. 157 (2018) 53–62. doi:https://doi.org/10.1016/j.polymdegradstab.2018.09.022.
URL https://www.sciencedirect.com/science/article/pii/S0141391018303021

[30] D. Chelazzi, D. Badillo-Sanchez, R. Giorgi, A. Cincinelli, P. Baglioni, Self-regenerated silk fibroin with controlled crystallinity for the reinforcement of silk, J. Coll. Interf. Sci. 576 (2020) 230–240. doi:https://doi.org/10.1016/j.jcis.2020.04.114.
URL https://www.sciencedirect.com/science/article/pii/S0021979720305786

[31] S. A. Rogers, In search of physical meaning: defining transient parameters for nonlinear viscoelasticity, Rheol. Acta 56 (5) (2017) 501–525. doi:10.1007/s00397-017-1008-1.
URL https://doi.org/10.1007/s00397-017-1008-1

[32] G. J. Donley, J. R. de Bruyn, G. H. McKinley, S. A. Rogers, Time-resolved dynamics of the yielding transition in soft materials, J. Non-Newton. Fluid Mech. 264 (2019) 117–134. doi:https://doi.org/10.1016/j.jnnfm.2018.10.003.
URL https://www.sciencedirect.com/science/article/pii/S0377025718302155

[33] S. A. Rogers, A sequence of physical processes determined and quantified in LAOS: An instantaneous local 2D/3D approach, J. Rheol. 56 (5) (2012) 1129–1151. doi:10.1122/1.4726083.
URL https://doi.org/10.1122/1.4726083

[34] F. Frenet, Sur les courbes à double courbure., J. Math. Pures Appl. (1852) 437–447.
URL http://eudml.org/doc/233946

[35] J.-A. Serret, Sur quelques formules relatives à la théorie des courbes à double courbure., J. Math. Pures Appl. (1851) 193–207.
URL http://eudml.org/doc/235002

[36] M. Laurati, S. U. Egelhaaf, G. Petekidis, Nonlinear rheology of colloidal gels with intermediate volume fraction, J. Rheol. 55 (3) (2011) 673–706. doi:http://dx.doi.org/10.1122/1.3571554.

[37] M. Laurati, S. U. Egelhaaf, G. Petekidis, Plastic rearrangements in colloidal gels investigated by LAOS and LS-Echo, J. Rheol. 58 (5) (2014) 1395–1417. doi:10.1122/1.4872059.
URL https://doi.org/10.1122/1.4872059

[38] N. Koumakis, G. Petekidis, Two step yielding in attractive colloids: transition from gels to attractive glasses, Soft Matter 7 (2011) 2456–2470. doi:10.1039/C0SM00957A.
URL http://dx.doi.org/10.1039/C0SM00957A

[39] N. Koumakis, E. Moghimi, R. Besseling, W. C. K. Poon, J. F. Brady, G. Petekidis, Tuning colloidal gels by shear, Soft Matter 11 (2015) 4640–4648. doi:10.1039/C5SM00411J.
URL http://dx.doi.org/10.1039/C5SM00411J

[40] L. C. Johnson, B. J. Landrum, R. N. Zia, Yield of reversible colloidal gels during flow start-up: release from kinetic arrest, Soft Matter 14 (2018) 5048–5068. doi:10.1039/C8SM00109J.
URL http://dx.doi.org/10.1039/C8SM00109J

[41] J. D. Park, K. H. Ahn, N. J. Wagner, Structure-rheology relationship for a homogeneous colloidal gel under shear startup, J. Rheol. 61 (1) (2016) 117–137. doi:10.1122/1.4971993.
URL https://doi.org/10.1122/1.4971993

[42] M. Kim, J.-E. Bae, N. Kang, K. Soo Cho, Extraction of viscoelastic functions from creep data with ringing, J. Rheol. 59 (1) (2014) 237–252. doi:10.1122/1.4904394.
URL https://doi.org/10.1122/1.4904394

[43] C. Cianci, D. Chelazzi, G. Poggi, F. Modi, R. Giorgi, M. Laurati, Hybrid fibroin-nanocellulose composites for the consolidation of aged silk, Coll. Surf. A in press (2021). doi:10.1016/j.colsurfa.2021.127944.

[44] C. Macosko, R. Larson, K. (Firm), Rheology: Principles, Measurements, and Applications, Advances in interfacial engineering series, VCH, 1994.
URL https://books.google.it/books?id=XXspAQAAMAAJ

[45] T. Sentjabrskaja, J. Hendricks, A. R. Jacob, G. Petekidis, S. U. Egelhaaf, M. Laurati, Binary colloidal glasses under transient stress- and strain-controlled shear, J. Rheol. 62 (1) (2018) 149–159. doi:10.1122/1.5009193.
URL https://doi.org/10.1122/1.5009193

[46] M. Laurati, G. Petekidis, N. Koumakis, F. Cardinaux, A. B. Schofield, J. M. Brader, M. Fuchs, S. U. Egelhaaf, Structure, dynamics, and rheology of colloid-polymer mixtures: From liquids to gels, J. Chem. Phys. 130 (13) (2009) –. doi:http://dx.doi.org/10.1063/1.3103889.

[47] A. Zaccone, H. Wu, E. Del Gado, Elasticity of arrested short-ranged attractive colloids: Homogeneous and heterogeneous glasses, Phys. Rev. Lett. 103 (2009) 208301. doi:10.1103/PhysRevLett.103.208301.
URL https://link.aps.org/doi/10.1103/PhysRevLett.103.208301

[48] L. C. Johnson, R. N. Zia, E. Moghimi, G. Petekidis, Influence of structure on the linear response rheology of colloidal gels, J. Rheol. 63 (4) (2019) 583–608. arXiv:https://doi.org/10.1122/1.5082796, doi:10.1122/1.5082796.
URL https://doi.org/10.1122/1.5082796

[49] R. Tanaka, Y. Kashiwagi, Y. Okada, T. Inoue, Viscoelastic Relaxation of Cellulose Nanocrystals in Fluids: Contributions of Microscopic Internal Motions to Flexibility, Biomacromolecules 21 (2) (2020) 408–417. doi:10.1021/acs.biomac.9b00943.
URL https://doi.org/10.1021/acs.biomac.9b00943

[50] M. Dinkgreve, J. Paredes, M. M. Denn, D. Bonn, On different ways of measuring "the" yield stress, J. Non-Newton. Fluid Mech. 238 (2016) 233–241. doi:https://doi.org/10.1016/j.jnnfm.2016.11.001.
URL https://www.sciencedirect.com/science/article/pii/S0377025716302774

[51] R. R. Fernandes, D. E. V. Andrade, A. T. Franco, C. O. R. Negrão, The yielding and the linear-to-nonlinear viscoelastic transition of an elastoviscoplastic material, J. Rheol. 61 (5) (2017) 893–903. doi:10.1122/1.4991803.
URL https://doi.org/10.1122/1.4991803

[52] A. Le Grand, G. Petekidis, Effects of particle softness on the rheology and yielding of colloidal glasses, Rheol. Acta 47 (5) (2008) 579–590. doi:10.1007/s00397-007-0254-z.
URL https://doi.org/10.1007/s00397-007-0254-z

[53] G. J. Donley, P. K. Singh, A. Shetty, S. A. Rogers, Elucidating the g" overshoot in soft materials with a yield transition via a time-resolved experimental strain decomposition, Proc. Nat. Acad. Sci. 117 (36) (2020) 21945–21952. arXiv:https://www.pnas.org/content/117/36/21945.full.pdf, doi:10.1073/pnas.2003869117.
URL https://www.pnas.org/content/117/36/21945

[54] W. Philippoff, Vibrational Measurements with Large Amplitudes, Trans. Soc. Rheol. 10 (1) (1966) 317–334. doi:10.1122/1.549049.
URL https://doi.org/10.1122/1.549049

[55] K. Hyun, M. Wilhelm, C. O. Klein, K. S. Cho, J. G. Nam, K. H. Ahn, S. J. Lee, R. H. Ewoldt, G. H. McKinley, A review of nonlinear oscillatory shear tests: Analysis and application of large amplitude oscillatory shear (LAOS), Prog. Polym. Sci. 36 (12) (2011) 1697 – 1753.

[56] D. V. Denisov, M. T. Dang, B. Struth, A. Zaccone, G. H. Wegdam, P. Schall, Sharp symmetry-change marks the mechanical failure transition of glasses, Sci. Rep. 5 (1) (2015) 14359. doi:10.1038/srep14359.
URL https://doi.org/10.1038/srep14359